



# Relating bed character and subglacial morphology using seismic data from Thwaites Glacier, West Antarctica

Atsuhiko Muto<sup>a,\*</sup>, Sridhar Anandakrishnan<sup>b</sup>, Richard B. Alley<sup>b</sup>, Huw J. Horgan<sup>c</sup>, Byron R. Parizek<sup>b,d</sup>, Stephen Koellner<sup>e</sup>, Knut Christianson<sup>f</sup>, Nicholas Holschuh<sup>f</sup>

<sup>a</sup> Dept. of Earth and Environmental Science, Temple University, Philadelphia, PA, USA

<sup>b</sup> Dept. of Geosciences and the Earth and Environmental Systems Institute, The Pennsylvania State University, University Park, PA 16802, USA

<sup>c</sup> Antarctic Research Center, Victoria University of Wellington, Wellington, New Zealand

<sup>d</sup> Geosciences and Mathematics, The Pennsylvania State University DuBois, DuBois, PA, USA

<sup>e</sup> Dept. of Mathematics, The Pennsylvania State University, University Park, PA 16802, USA

<sup>f</sup> Dept. of Earth and Space Sciences, University of Washington, Seattle, WA, USA

## ARTICLE INFO

### Article history:

Received 7 September 2018

Received in revised form 6 December 2018

Accepted 11 December 2018

Available online 19 December 2018

Editor: M. Ishii

### Keywords:

Thwaites Glacier  
West Antarctica  
seismic reflectivity  
bed character  
till properties

## ABSTRACT

Seismic measurements on Thwaites Glacier show a spatially variable bed character, with implications for ice-sheet stability. The West Antarctic Ice Sheet is losing mass rapidly through outlet glaciers and ice streams in the Amundsen Sea Embayment, including Thwaites Glacier, where limited observations and modeling suggest that ice-flow rates depend on bed properties. Here we characterize bed properties of Thwaites Glacier based on amplitude analysis of reflection-seismic data from a ~40-km-long profile collected in the approximate flow direction and two ~10-km-long profiles transverse to flow. The upstream portion of the seismic profile reveals a ~12-km long sedimentary basin with ice-flow-aligned bedforms capped by a continuous till layer that is likely soft and deforming (porosity ~0.4–0.45), with several locations where water has pooled at the bed. Downstream of the sedimentary basin, the bed rises by ~400 m over ~25 km into subglacial highlands. Our seismic survey of these subglacial highlands reveals strong spatial variations in bed character across rugged topography (~200 m amplitude at ~2- to 5-km wavelength) resembling crag-and-tails. Till on the stoss sides (facing upglacier) of topographic highs is more consolidated (porosity ~0.3–0.35 or lower), whereas the lee sides (facing downglacier) and flat regions exhibit porosity similar to the till of the upstream sedimentary basin. Modeling studies could use the observed correlation between bed character and bed aspect and slope to extend our observations to other parts of Thwaites Glacier, resulting in more-realistic models of future grounding-line retreat. Our findings highlight the need for more geophysical constraints on bed properties for important outlets in Antarctica and Greenland.

© 2018 Published by Elsevier B.V.

## 1. Introduction

Deglaciation of the marine basins of the West Antarctic Ice Sheet (WAIS) would raise global sea level by about 3.3 m (Bamber et al., 2009). A large fraction of WAIS drains through the glaciers of the Amundsen Sea Embayment (ASE), where satellite observations show accelerations in grounding-line retreat and ice-mass loss in the past decade (e.g., Mouginot et al., 2014; Harig and Simons, 2015). Thwaites Glacier (TG) is the largest ice reservoir in the ASE and lost  $89 \pm 23$  Gt/yr or  $0.26 \pm 0.06$  mm/yr of sea-level-equivalent mass between 2008 and 2015 (Gardner et al., 2018). Models show

that deglaciation of other marine basins of WAIS could be initiated by major retreat of TG, and some models even suggest that the unstable retreat of TG and WAIS has already started (Joughin et al., 2014; DeConto and Pollard, 2016).

The ongoing acceleration of the ice-mass loss from the ASE is largely attributed to the reduced buttressing of the grounded ice by ice shelves due to their melting and thinning, caused by the sub-shelf intrusion of relatively warm Circumpolar Deep Water (e.g., Christianson et al., 2016; Jenkins et al., 2016). How the grounded ice responds to such ocean forcing and whether it will lead to unstable retreat critically depends on the geometry and the character of the bed around the grounding zone (e.g., Parizek et al., 2013; Nias et al., 2016). The current TG grounding line is partially stabilized on a bedrock sill (Joughin et al., 2014). Parizek et al. (2013) showed that when the bed was treated as viscous,

\* Corresponding author.

E-mail address: amuto@temple.edu (A. Muto).

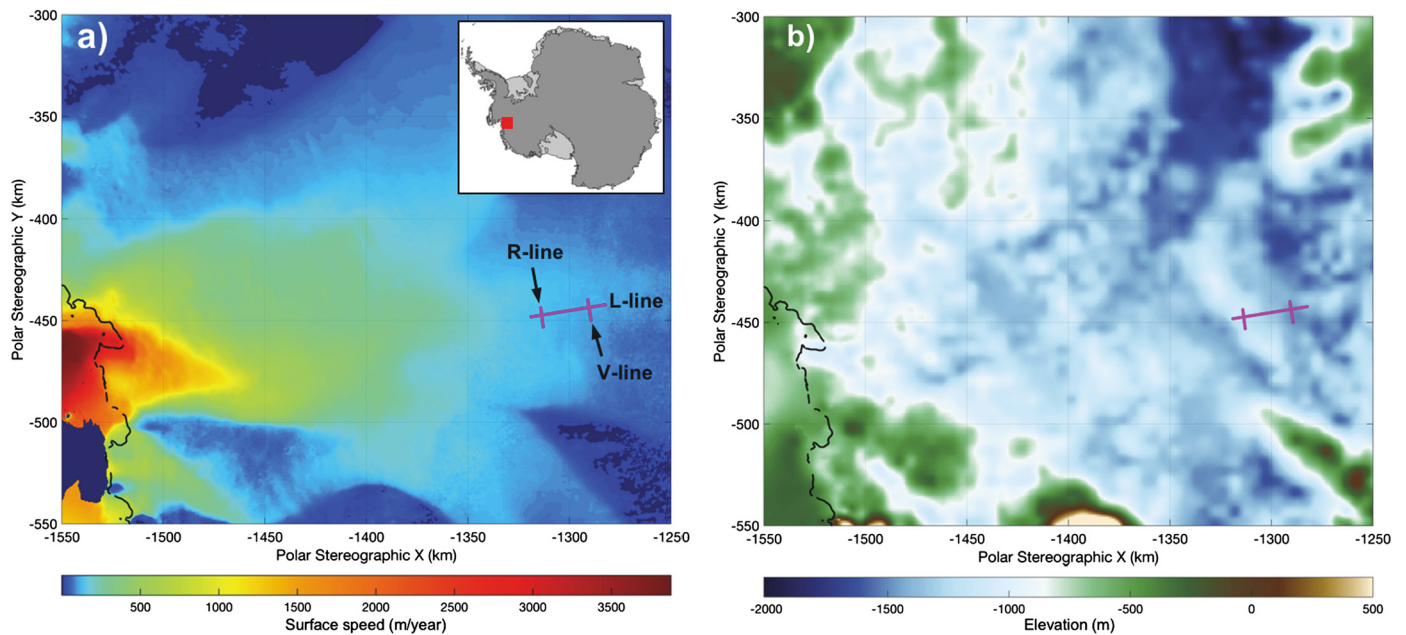


**Fig. 1.** Maps of Thwaites Glacier (TG) showing the locations of our seismic-survey lines (pink solid lines). (a) Surface-speed map of TG from NASA MEaSUREs InSAR-derived data (Rignot et al., 2017). The black line is the NASA InSAR-derived grounding line in 2011 (Rignot et al., 2016). The inset map shows the location of TG in Antarctica. (b) Bed-elevation map of TG from Bedmap2 (Fretwell et al., 2013). This figure was created using the Antarctic Mapping Tools (Greene et al., 2017). (For interpretation of the colors in the figure(s), the reader is referred to the web version of this article.)

as expected for sliding over a hard bed (Weertman, 1957), the thinning in response to ocean warming is localized near the coast, causing retreat from the bedrock sill into deep basins followed by rapid deglaciation. However, Parizek et al. (2013) also showed that plastic deformation at the bed, as expected for soft till, reduces coastal thinning by rapidly tapping inland ice, delaying or eliminating retreat from the stabilizing sill and the resulting ice-sheet collapse.

The distribution of bed types beneath WAIS is poorly known, leading to uncertainties in the timing and rate of future TG retreat. However, unknown bed properties can be constrained using reflection-seismic data. Here we analyze the normal-incidence reflectivity of the glacier bed from ~60 km of active-source seismic data collected in the upper TG (Fig. 1), finding spatial variations in bed character that are correlated with the stoss (facing upglacier) and lee (facing downglacier) sides of subglacial ridges oriented in the ice flow direction. Related modeling (Koellner et al., 2018) shows that TG stability is affected if similar patterns exist near the modern grounding zone, motivating additional observations.

## 2. Data and methods

### 2.1. Reflection-seismic profiling

During December 2008 and January 2009, multichannel reflection-seismic data were collected on the main trunk of upper TG (Fig. 1), with a ~37-km-long profile (labeled the L-line) approximately along the ice-flow direction, crossed by two ~10-km-long profiles perpendicular to the L-line and transverse to ice flow (labeled V-, and R-lines). The same dataset was used to study the crystal-orientation fabric as revealed by englacial seismic reflectivity (Horgan et al., 2011), and the details on the data collection can be found in that paper.

We prepared seismic sections using standard multichannel-processing techniques for Antarctic reflection-seismic data (e.g., Horgan et al., 2011; Smith et al., 2013; Luthra et al., 2017). Pre-stack processing included removal of noisy and bad traces, static corrections to adjust for shot-hole and surface-elevation variations,

and band-pass and frequency-wavenumber (FK) filtering to reduce residual broadband noise and the direct-arrival and ground-roll energy. We also applied predictive deconvolution to suppress the energy of the “ghost” reflections (those that arise from energy that travels upward from the explosive sources, which were buried ~40–50 m in the firn, before reflecting to the bed and back to the sensors, arriving shortly after the primary reflections from energy propagating down from the sources). Shot data were then sorted into common depth point (CDP) gathers and the arrival times corrected for receiver distance (normal moveout, or NMO) before stacking. After stacking, we performed finite-difference migration to position dipping reflectors correctly and to reduce diffraction energy. The peak frequency of the primary reflections is ~150 Hz, which corresponds to a vertical resolution in ice of ~6.4 m (using the Rayleigh criterion of 1/4 wavelength) and a Fresnel-zone width of ~365 m at the average depth of ~2600 m (Fig. 2a).

### 2.2. Seismic-amplitude analysis

We applied a separate processing flow for the seismic-amplitude analysis to derive the normal-incidence reflection coefficient ( $R_0$ ) and the bed acoustic impedance ( $Z_b$ ). Here, our processing was limited to removing noisy traces and applying static corrections and frequency filtering; these steps preserve the true amplitudes of the reflections. We determined  $R_0$  from the source and reflection amplitudes (Holland and Anandakrishnan, 2009):

$$R_0 = \frac{A_1}{A_0} \frac{1}{\gamma} e^{\alpha d_1}, \quad (1)$$

where  $A_0$  and  $A_1$  are the amplitudes of the source and the recorded primary reflection, respectively,  $\gamma$  is the path amplitude factor (Medwin and Clay, 1998), which accounts for the geometrical spreading through firn and ice,  $\alpha$  is the attenuation constant and  $d_1$  is the distance along the path of the primary reflection. The source amplitude ( $A_0$ ) was determined by applying the direct-path method of Holland and Anandakrishnan (2009), which uses pairs of arrivals for which the ray-path length of one is double the other. We chose the direct-path method rather than the multiple-

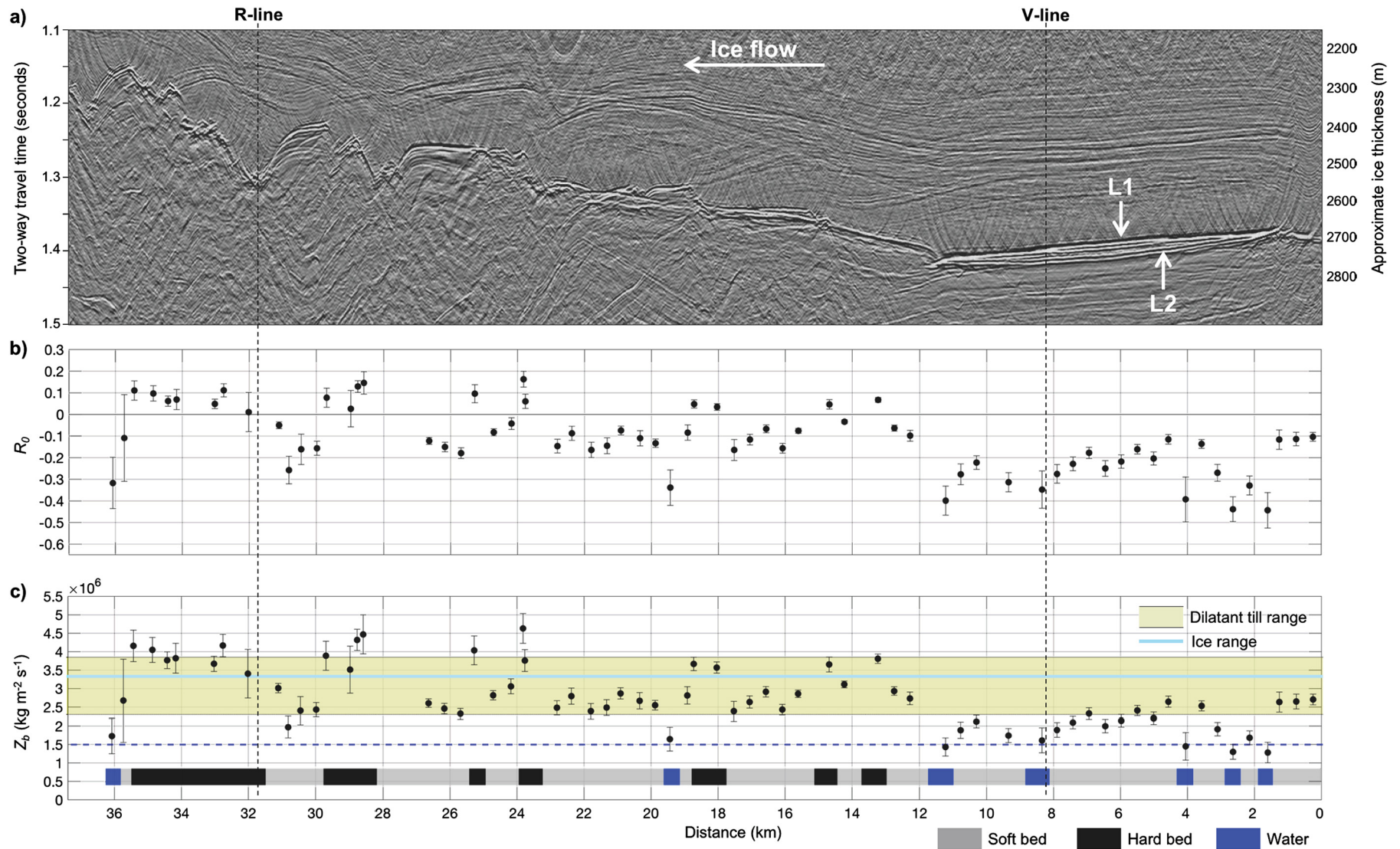


**Fig. 2.** (a) Stacked, migrated seismic section of the L-line profile. Automatic gain control with the a 50-millisecond window has been applied to enhance the image quality for display purposes. The ice thickness indicated on the right are from using a stacking velocity of 3810 m/s. R-line and V-line indicate where the transverse profiles intersect. L1 and L2 indicate the two strong bed reflections (see text for details). (b) Normal-incidence reflection coefficient ( $R_0$ ). (c) The bed acoustic impedance ( $Z_b$ ). Yellow band indicates the possible values of deforming till (Atré and Bentley, 1993). Cyan band indicates the range of the acoustic impedance of ice (Atré and Bentley, 1993). Blue dotted line is the acoustic impedance of water. The bar at the bottom shows our interpretation of the bed type.



bounce method that is more commonly used (e.g., Smith, 2007; Brisbourne et al., 2017) because our data lacked clear multiple reflections from the bed in most shots. The path amplitude factor ( $\gamma$ ) and the primary-ray-path length ( $d_1$ ) were determined by ray tracing through a one-dimensional velocity model of the glacier that includes both firn and ice (Horgan et al., 2011). We used an attenuation constant  $\alpha = 2.7 \times 10^{-4} \text{ m}^{-1}$  (Horgan et al., 2011). Horgan et al. (2011) used a range of  $\alpha$  from 2 to  $4 \times 10^{-4} \text{ m}^{-1}$  in their uncertainty estimate; here, we assigned a slightly larger uncertainty of  $\pm 1.35 \times 10^{-4} \text{ m}^{-1}$  (50%).

The wavelet of the direct arrival is similar to a zero-phase Ricker wave, with a high-amplitude main lobe and lower-amplitude side lobes (Sheriff and Geldart, 1995). The majority of primary bed reflections have similar wavelets, although in some places the primary reflection is followed closely by later arrivals. Therefore, we measured the amplitude of the main lobe only, following previous studies (e.g., Smith et al., 2002; Booth et al., 2012), rather than calculating the root-mean-square time-window amplitudes to capture the whole wavelet (e.g., Horgan et al., 2011; Brisbourne et al., 2017).

We used shot gathers that included source-to-receiver offsets of  $-480$  to  $460$  m. For ice-bottom dips less than  $5^\circ$ , this offset range leads to incidence angles of the primary bed reflection less than  $10^\circ$ , which was the case for the majority of the shots used. Traces with incidence angle  $>10^\circ$  were excluded from the analysis. We estimated the source amplitude ( $A_0$ ) of each shot as the average of  $A_0$  calculated from all available arrival pairs within a shot gather with the standard deviation taken as its uncertainty (minimum of 3 pairs of traces with a mean of 8 pairs). Similarly, we estimated the primary-reflection amplitude ( $A_1$ ) and its uncertainty for each shot as the average and the standard deviation, respectively, of all available traces within a shot gather (minimum of 18 traces with a mean of 41 traces). The uncertainty in  $R_0$  for each shot was calculated by propagating the uncertainty in  $A_0$ ,  $A_1$  and  $\alpha$  in equation (1) (e.g., Taylor and Kuyatt, 1994).

After determining  $R_0$ , the bed acoustic impedance ( $Z_b$ ) was calculated as (e.g., Smith, 2007; Luthra et al., 2017)

$$Z_b = Z_{ice} \frac{(1 + R_0)}{(1 - R_0)}. \quad (2)$$

We assumed  $Z_{ice} = 3.33 \pm 0.04 \times 10^6 \text{ kg m}^{-2} \text{ s}^{-1}$ , following Atré and Bentley (1993). This value was derived for Whillans and Kamb Ice Streams (formerly Ice Streams B and C, respectively) assuming a 5-m-thick layer of basal ice at the pressure-melting point. Although there are no available temperature measurements for this region of TG, observations (Schroeder et al., 2014a) and models (e.g., Joughin et al., 2009) suggest that the base of the ice is at the pressure-melting point. Although we do not know the thickness of any temperate ice at this point, we follow previous seismic studies of the neighboring Pine Island Glacier (Smith et al., 2013; Brisbourne et al., 2017) in assuming that conditions are similar and well-represented by the  $Z_{ice}$  estimate of Atré and Bentley (1993). The uncertainty in  $Z_b$  was calculated by propagating the uncertainty in  $R_0$  and  $Z_{ice}$  in equation (2).

### 3. Results

#### 3.1. Seismic profiles

Fig. 2a shows a stacked section of the along-flow L-line, highlighting a relatively smooth, flat subglacial basin that is approximately 12-km long. Flow then encounters subglacial highlands, where the bed rises by  $\sim 400$  m over  $\sim 25$  km with topographic relief of up to  $\sim 200$  m at several-kilometer length scales.

In the basin, we observe a strong bed reflection (L1) at a two-way travel time of  $\sim 1.4$  s. A second arrival (L2) directly after L1

is first apparent at km 2 and, by km 6.5, is about 20 milliseconds delayed relative to the L1 arrival. L2 merges back into L1 by km 11.5 (Fig. 2a). We interpret both of these as off-axis arrivals (side swipe) due to non-planar and non-horizontal cross-line bed topography. For an observer looking downglacier, our transverse V-line shows the bed rising from a trough on the left of our along-flow L-line, to a ridge on the right (Fig. 3a). The first, L1 reflector likely comes from this slope to the right of the L-line near the top of the ridge, with the L2 reflection from just beyond the axis of the trough. Because the reflector complexity can be explained by local topography instead of sub-ice-bottom structures, we do not attempt to estimate till thickness or other sub-ice-bottom geologic structures.

In the downstream subglacial highlands, we observe bedforms that are between 2- and 5-km long and up to  $\sim 200$ -m high (from km 20 to 36), with steeper stoss sides and smooth, lower-angle or horizontal lee sides (Fig. 2a). These are similar to some bedforms observed below the onset region of Rutford Ice Stream (King et al., 2007; Smith et al., 2007). We also see more than one coherent arrival in some places, e.g., at km 15–16 and 25–27. The L-line and the transverse R-line (Fig. 4a) show that the topography is rougher in the highlands than in the basin, and that roughness is greater transverse to flow on the R-line than along flow on the L-line. This indicates that at least some of the coherent arrivals are likely off-axis reflections. Ray-path modeling using both lines and the radar-derived bed topography may allow reflectors to be attributed to particular off-axis topographic features, but we do not attempt that here. We thus do not interpret any sub-ice-bottom structures because of the possibility that they are off-axis ice-bottom reflections, and we caution that some off-axis ambiguity is present in our results.

#### 3.2. $R_0$ and $Z_b$ profiles

Estimates of the normal-incidence reflection coefficient ( $R_0$ ) and the acoustic impedance ( $Z_b$ ) for each profile are shown in panels b and c, respectively, of Figs. 2 to 4. For the  $Z_b$  profiles, we also plot the generally accepted range of acoustic impedances from a subglacial layer consisting of dilatant, deforming till and for basal ice, and the preferred value for water (Atré and Bentley, 1993; Smith, 1997). Values of  $R_0 > 0$  and  $Z_b > 3.33 \times 10^6 \text{ kg m}^{-2} \text{ s}^{-1}$  correspond to a till porosity of  $\sim 0.3$ – $0.35$  and lower, and include lodged, non-deforming till. We thus refer to regions of  $R_0 > 0$  and  $Z_b > 3.33 \times 10^6 \text{ kg m}^{-2} \text{ s}^{-1}$  as “hard beds” and  $R_0 < 0$  and  $2.0 \times 10^6 < Z_b < 3.33 \times 10^6 \text{ kg m}^{-2} \text{ s}^{-1}$  as “soft beds” in panel c of Figs. 2 to 4, noting that even softer beds ( $Z_b$  lower than the dilatant-till range of Atré and Bentley (1993) but not as low as that of water, e.g., Vaughan et al., 2003; Peters et al., 2008), and intermediate beds between “soft” and “hard” ( $R_0 \sim 0 \pm 0.1$ ; Luthra et al., 2017) might occur. Also, there are several locations where we observed the polarity of the primary reflection switching within a shot gather, most notable of which are at km 35.5 in the L-line ( $R_0 = -0.11 \pm 0.20$ ) and at km 1.9 in the V-line ( $R_0 = -0.23 \pm 0.24$ ), showing our ability to resolve rapid spatial variations in bed type.

The signs of the reflection coefficients ( $R_0$ ) in the basin are consistently negative along both the L-line (Fig. 2b) and the V-line (Fig. 3b) profiles. Along the L-line, values of  $R_0 \sim -0.1$  at the upstream end of the basin, decreasing to  $R_0 \sim -0.2$  to  $-0.3$  towards the downstream end. There are also several locations with  $R_0$  between  $-0.35$  and  $-0.45$ , which suggest the presence of water, discussed further below. The V-line profile shows a similar range of values. The resulting bed-acoustic-impedance estimates ( $Z_b$ ) in the basin range mostly from about  $1.7$  to  $3 \times 10^6 \text{ kg m}^{-2} \text{ s}^{-1}$  (Fig. 3c), consistent with the presence of deforming till, including till softer than that found on Whillans Ice Stream (Blankenship et al., 1987;

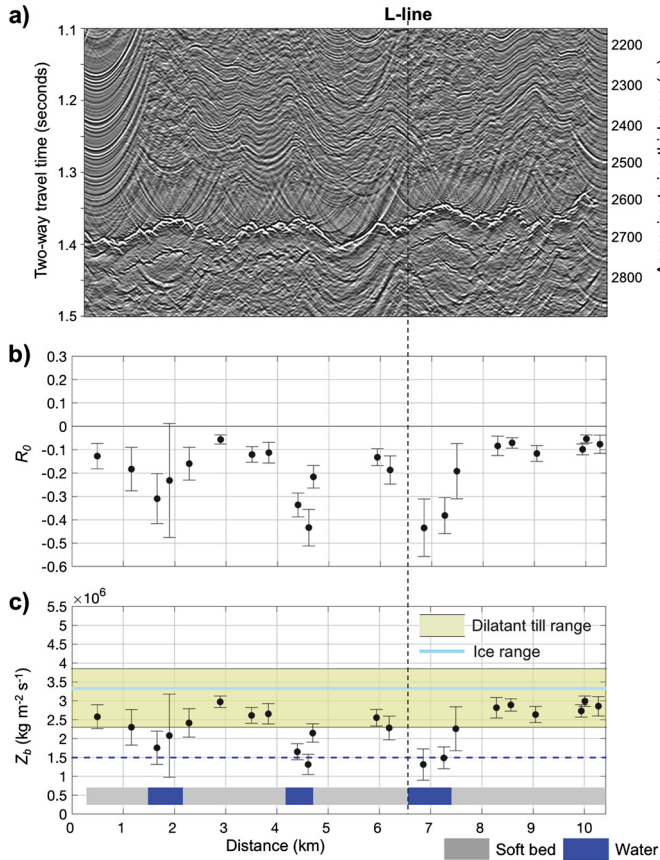


Fig. 3. Same as Fig. 2 but for V-line profile. Ice flow into the page.

Atre and Bentley, 1993). These values of  $R_0$  and  $Z_b$  are observed both in the troughs and on the ridges of cross-flow topography, suggesting a continuous dilatant till. The bed in the entire basin is, therefore, soft with several locations of pooled water.

In the subglacial highlands, we see both negative-polarity reflections indicative of soft beds, and positive-polarity reflections showing hard beds. These variations appear correlated with the topography, except on the ~3-km-long slope immediately downstream of the basin (km 11.5–14.5) where we see both soft and hard beds. After this initial upslope into the highlands, hard beds are observed on the upslope or stoss sides of the bedrock bumps, and soft beds on the horizontal- to downstream-sloping lee sides. Along the transverse R-line, the presence of soft and hard beds appears uncorrelated with topography, indicating that the bed character is controlled more by along-flow stoss/lee position than by transverse (trough, flank or crest) position.

Discrete, seismically resolvable water layers (small lakes) are suggested along all three profiles, with the largest being ~1 km long. Some but not all of these occur where local lows in the bed topography favor water pooling (e.g., km 11.7 and km 36 on the L-line). Full 3-d calculation of hydrologic potential would be needed to confirm water-flow convergence (e.g., Smith et al., 2017). But, our data indicate that water in thicknesses exceeding our seismic resolution (~2.4 m in water at 1432 ms<sup>-1</sup> (King et al., 2004) and the dominant frequency of 150 Hz) is scattered in the upper reaches of TG.

A summary of the normal-incidence reflection coefficients  $R_0$  is given in the histogram in Fig. 5. Overall, the data fall into three modes: water (values less than ~-0.3); soft tills (the other negative values), and harder material (positive values, likely from compacted till or weakly lithified sedimentary rock). The usual caveats for seismic surveys should be borne in mind, although we believe

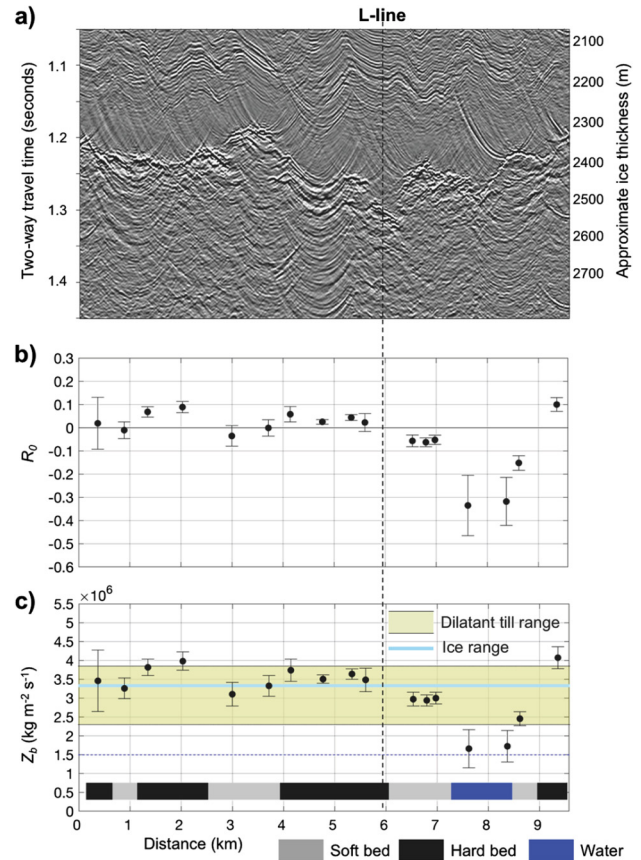


Fig. 4. Same as Fig. 2 but for R-line profile. Ice flow into the page.

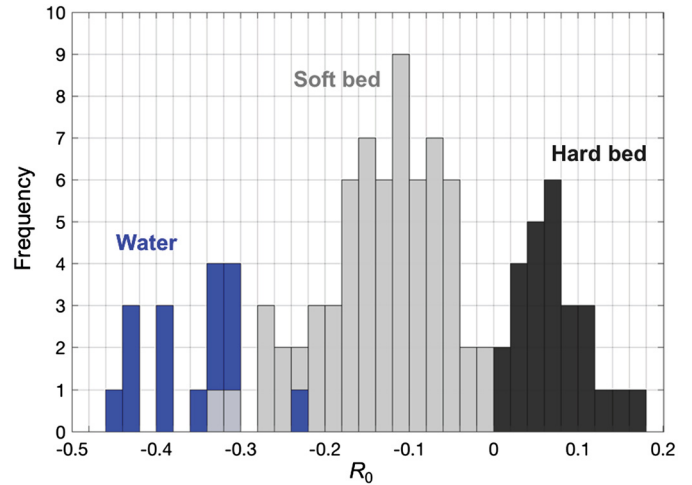


Fig. 5. Histogram of observed normal-incidence reflection coefficient  $R_0$  from all three survey lines combined. The number of samples is 107. Three colors correspond to the interpreted bed types shown in Figs. 2c, 3c and 4c.

they do not affect the interpretations here. Seismically thin layers of dilatant till—less than 1/6 the seismic wavelength—on top of lodged till are not independently resolvable (Booth et al., 2012). In our case, with dominant frequency of 150 Hz, this is ~2 m in till at 1800 ms<sup>-1</sup>, and ~4 m in clean ice. Hence, a thin layer of soft till in the subglacial highlands would not be resolved. Values of  $R_0$  and  $Z_b$  intermediate between till and water ( $R_0 \sim -0.3$  to  $-0.2$  and  $Z_b \sim 2.0$  to  $2.2 \times 10^6$  kg m<sup>-2</sup> s<sup>-1</sup>) may result from a seismically thin layer of water between ice and till. Reflections from the top (ice/water interface) and the bottom (water/till interface) of a water layer less than ~1-m thick can destructively interfere, re-

sulting in an  $R_0$  higher than the theoretical  $-0.4$  for the ice/water interface (King et al., 2004). For example, the reflection amplitude would be  $\sim 70\%$  of the theoretical ice/water-interface value (i.e.,  $R_0 \sim -0.28$ ) if the water layer is 0.4– to 0.6-m thick for the dominant frequency of 150 Hz, and remains perturbed down to a water thickness of  $\sim 0.2$  m (King et al., 2004). It is possible that our observations of  $R_0 \sim -0.3$  to  $-0.2$  resulted from water layers of  $\sim 0.2$  to 0.6 m. King et al. (2004) also showed that reflections from the top and the bottom of a water layer  $\sim 0.8$ - to 1.5-m thick can constructively interfere, resulting in  $R_0$  that are 10 to 20% lower than  $-0.4$ . This could explain our observations of  $R_0 \sim -0.43$  to  $-0.44$  at km 1.6 and 2.6 on the L-line (Fig. 2b) and km 4.6 and 6.8 on the V-line (Fig. 3b).

In a number of shot gathers, we observed primary reflections that deviated from simple, Ricker-like wavelets with one main lobe and two side lobes, appearing to share the trailing side lobe with the leading one of a closely-following arrival. As explained in section 2.2, our choice of measuring the amplitude of the first main lobe is intended to avoid interference effects from later arrivals. However, we cannot totally rule out the possibility that the main lobe we picked may include interference effects, such that our calculated reflectivity may deviate from the true amplitude of the primary bed reflection.

Basal ice often contains debris, which increases the density and seismic velocity. We did not find identifiable reflections from seismically thick debris-laden ice above the bed, but we cannot rule out the possibility of a seismically thick layer with low but nonzero debris concentration, or a seismically thin layer with higher concentration, either of which would have some effect on our results. As an example, a thick layer of dirty ice with 5% sediment (density =  $1000 \text{ kg/m}^3$ , with sediment density of  $2500 \text{ kg/m}^3$ ) would have an acoustic impedance ( $Z_{ice}$ ) of  $3.63 \times 10^6 \text{ kg m}^{-2} \text{ s}^{-1}$ , which, if ignored, would lead to an underestimate of  $Z_b$  by  $\sim 10\%$ . This might explain intermediate values, which should actually fall in the dilatant-till range of Atré and Bentley (1993). We note, however, that our distinction of hard versus soft bed is mainly based on the polarity of the reflection, which would not be changed by such a debris-bearing layer. Furthermore, the bed types we find—localized water, extensive dilated soft till, and harder till or sediment—are consistent with results from other West Antarctic sites (e.g., King et al., 2004; Smith et al., 2013; Brisbourne et al., 2017; Luthra et al., 2017).

The seismic data thus show that the bed is primarily either “hard” (consolidated till or sediment), “soft” (dilated, deforming till), or locally decoupled from the bed by a seismically resolvable water layer. Hard beds occur on stoss sides of topography, with soft beds on lee sides, including the  $\sim 12$  km long basin at the up-glacier end of our seismic line and the kilometers-scale lee sides of topography in the subglacial highlands. Water is localized where sharp bed-slope gradients favor water-flow convergence. We note that we picked and analyzed only the first ice-bottom arrival regardless of whether this arrival came from on- or off-axis. As we explained above, our most significant result does not rely on the precise location of observed  $R_0$  and  $Z_b$  laterally.

#### 4. Discussion

Our seismic observations indicate that diverse bedforms elongated parallel to ice flow occur under the upper reaches of TG. In the basin, we see smooth, continuous reflectors in the along-flow L-line profile (Fig. 2a), and crests and troughs along the transverse V-line profile (Fig. 3a). Seismic reflections from both crests and troughs indicate soft and likely deforming till, except where pockets of water occur. These features are  $\sim 500$ - to  $1500$ -m wide and  $\sim 50$ - to  $60$ -m high, similar to or somewhat larger than mega-scale glacial lineations (MSGLs) inferred from airborne-radar images and

specularity for upstream TG including our study area (Schroeder et al., 2014b), and also observed beneath other modern (King et al., 2009; Bingham et al., 2017) and paleo-ice streams (Graham et al., 2009; Spagnolo et al., 2017) in West Antarctica.

In the subglacial highlands, we observe bedforms of  $\sim 2$ - to  $5$ -km long in the L-line with steeper, hard-bedded stoss sides and smoother, horizontal to lower-angle soft-bedded lee sides (Fig. 2a). Across-flow crest-and-trough structures in the R-line (Fig. 4a) have higher relief than in the basin. These structures resemble crag-and-tail features described from many current and formerly glaciated regions including beneath Rutford Ice Stream (King et al., 2007) and beneath the Amundsen Sea (Graham et al., 2009; Nitsche et al., 2016). The airborne-radar data of Schroeder et al. (2014b), which are sensitive primarily to meter-scale features too small to be resolved in our seismic data, show lineated bedforms in both the basin and the highlands. Additional work to integrate radar and seismic data across spatial scales could yield further insights.

Ice flow in the Amundsen Sea embayment likely has been more-or-less steady for millennia or longer (Bingham et al., 2017), so the inferred till deformation in the upper reaches of TG suggests that till flux continues into downglacier reaches, and that similar features will be observed there. Joint interpretation of radar, seismic and ice-flow data will be required to test this and other hypotheses.

Physical understanding, laboratory and field data show that the “flow law” relating basal velocity ( $u_b$ ) to shear stress ( $\tau_b$ ) varies strongly depending on bed type. This relation is often written as a power-law,  $u_b = B\tau_b^m$ . On “hard” beds, ice may regelate (pressure melt and refreeze) around small obstacles generating linear behavior ( $m = 1$ ), creep around larger obstacles with moderate nonlinearity ( $m = 3$ ), or some combination of these with  $m = 2$  (Weertman, 1957). For soft beds, small strains produce strong nonlinearity ( $m \sim 7$ ; Rathbun et al., 2008), with additional strain generating extreme nonlinearity approaching perfect plasticity ( $m \rightarrow \infty$ ) (e.g., Kamb, 1991; Tulaczyk et al., 2001; Rathbun et al., 2008); nonsteady forcing may “remold” tills and allow persistence of strong, rather than extreme, nonlinearity (Leeman et al., 2016). (The drag from water in subglacial lakes is so small that its viscous nature is unimportant. Also, for  $\tau_b$  above some upper limit that depends on bed geometry, a hard bed will transition to more-nearly-plastic behavior; Schoof, 2005.)

Inversion for basal drag from observed ice thickness, surface slope and surface velocity is a powerful tool for initialization of ice-flow models (e.g., MacAyeal, 1992; Morlighem et al., 2013). Such inversions have been conducted assuming linear-viscous, plastic, and intermediate beds, and are all similarly successful in matching the input data (e.g., Joughin et al., 2009, 2010). However, forward models using different degrees of basal nonlinearity can simulate very different future behavior (Joughin et al., 2010; Parizek et al., 2013; Koellner et al., 2018). Observations of time-evolving ice velocity could help identify the degree of basal nonlinearity (e.g., Walker et al., 2012), and use of deformation of internal radar reflectors through the ice thickness in addition to the surface topography may provide additional information (e.g., Holschuh et al., 2017), but applying these techniques is not yet practical in many cases.

The results here offer a possible way forward. For our along-flow survey line, stoss faces of topography have hard beds, and lee faces are soft till. Hence, stoss faces are expected to have nearly linear behavior, and lee faces more-nearly plastic. Even if a thin layer of soft sediment were present but unresolvable on the stoss faces, the form drag of the topography would have  $m = 3$  behavior (Weertman, 1957), much closer to linear than for the lee sides. However, the common occurrence of crag-and-tail features with hard upglacier faces and till tails on many length scales, as



noted above, favors the hypothesis that the stoss faces are “hard” at scales too small for resolution in the seismic data.

Targeted surface geophysics with borehole sampling would be ideal for testing the ideas here. Pending such studies, our results suggest that inversions for basal drag leading to prognostic modeling in our survey region should be conducted with the assumption that the bed exhibits nearly linear-viscous behavior on stoss faces where we find hard beds, and nearly plastic behavior on lee faces where we find soft beds. Coupling such analyses to traditional end-member treatments with linear and with plastic beds would give a central estimate and the uncertainty range. Furthermore, although additional seismic surveys should be used to extend our results to other parts of TG, it is reasonable to use ice-thickness data to identify stoss and lee slopes where seismic surveys have not yet been conducted, and to include the stoss-linear/lee-plastic model in future studies of TG stability. Areas ~50 and 100 km downstream of our seismic profiles show roughly east-west trending, ~10- to 20-km wide highlands between low-elevation basins (Fig. 1b), similar to those of the subglacial highlands of our study area. These may be areas where the stoss-linear/lee-plastic model may be applied.

## 5. Conclusion

Seismic data from upstream reaches of the main trunk of Thwaites Glacier show a long, smooth downslope with large lineated bedforms over ~12 km leading to a rising slope ~25 km long with higher-frequency topography (wavelengths of several km) resembling crag-and-tails. Spatial variations are observed in the phase and the amplitude of the normal-incidence reflections from this bed. Analyses of these reflections show several discrete regions of ponded water, together with widespread regions of “soft” bed consistent with deforming till, and of “hard” bed consistent with consolidated till or sediment.

The distribution of the different bed types is correlated to the basal topography. Hard regions occur on stoss (upglacier-facing) slopes of the higher-frequency topography, and soft regions on the lee slopes of that topography and on the long downslope, with water in places favorable for ponding.

As discussed above, physical models plus laboratory and field data from other sites suggest that the basal velocity of ice motion will increase as a small power of stress in hard-bed regions, and as a large power of stress in soft-bed regions. Furthermore, prognostic modeling suggests that proper specification of the basal flow law will affect assessments of ice-sheet stability and contributions to sea-level rise. We thus suggest, pending further data and hypothesis-testing, that inversions for basal drag used to inform prognostic modeling should be conducted assuming near-linear behavior on stoss faces and near-plastic behavior on lee faces, to supplement prior practice of assuming the entire bed is either nearly linear or nearly plastic.

## Acknowledgements

This work was supported by the US National Science Foundation under grants NSF-NERC-PLR-1738934 (A.M., S.A., R.B.A., B.R.P., K.C., N.H.), OPP-0424589 (S.A., R.B.A.), PLR-1443190 (B.R.P., S.J.K.), by the National Aeronautics and Space Administration under grant NNX15AH84G (A.M., B.R.P., S.J.K.) and by the Heising-Simons Foundation, Grant Agreement #2018-0769 (S.A., R.B.A., B.R.P.). We thank Mike Jayred from the Ice Drilling and Design Operations for leading the drilling of seismic-shot holes. We also thank J. MacGregor, L. Peters and D. Voigt for their help in data collection. We are also grateful for the field support provided by Raytheon Polar Services Company. Comments from two anonymous reviewers improved the

manuscript. The dataset used in this study is available through Mendeley Data and from the corresponding author upon request.

## References

- Atre, S.R., Bentley, C.R., 1993. Laterally varying basal conditions beneath Ice Streams B and C, West Antarctica. *J. Glaciol.* 39 (133), 507–514.
- Bamber, J.L., Riva, R.E.M., Vermeersen, B.L.A., Le Brocq, A.M., 2009. Reassessment of the potential sea-level rise from a collapse of the West Antarctic Ice Sheet. *Science* 324, 901–903. <https://doi.org/10.1126/science.1169335>.
- Bingham, R.G., Vaughan, D.G., King, E.C., Davies, D., Cornford, S.L., Smith, A.M., Arthern, R.L., Brisbourne, A.M., De Rydt, J., Graham, A.G.C., Spagnolo, M., Marsh, O.J., Shean, D.E., 2017. Diverse landscapes beneath Pine Island Glacier influence ice flow. *Nat. Commun.* 8 (1), 1–9. <https://doi.org/10.1038/s41467-017-01597-y>.
- Blankenship, D.D., Bentley, C.R., Rooney, S.T., Alley, R.B., 1987. Till beneath ice stream B: 1. Properties derived from seismic travel times. *J. Geophys. Res.* 92 (B9), 8903–8911. <https://doi.org/10.1029/JB092iB09p08903>.
- Booth, A.D., Clark, R.A., Kulesa, B., Murray, T., Carter, J., Doyle, S., Hubbard, A., 2012. Thin-layer effects in glaciological seismic amplitude-versus-angle (AVA) analysis: implications for characterising a subglacial till unit, Russell Glacier, West Greenland. *Cryosphere* 6 (4), 909–922. <https://doi.org/10.5194/tc-6-909-2012>.
- Brisbourne, A.M., Smith, A.M., Vaughan, D.G., King, E.C., Davies, D., Bingham, R.G., Smith, E.C., Nias, I.J., Rosier, S.H.R., 2017. Bed conditions of Pine Island Glacier, West Antarctica. *J. Geophys. Res., Earth Surf.* 122, 419–433. <https://doi.org/10.1002/2016JF004033>.
- Christianson, K., et al., 2016. Sensitivity of Pine Island Glacier to observed ocean forcing. *Geophys. Res. Lett.* 43, 10,817–10,825. <https://doi.org/10.1002/2016GL070500>.
- DeConto, R., Pollard, D., 2016. Contribution of Antarctica to past and future sea-level rise. *Nature* 531 (7596), 591–597. <https://doi.org/10.1038/nature17145>.
- Fretwell, P., et al., 2013. Bedmap2: improved ice bed, surface and thickness datasets for Antarctica. *Cryosphere* 7, 375–393. <https://doi.org/10.5194/tc-7-375-2013>.
- Gardner, A.S., Moholdt, G., Scambos, T., Fahnestock, M., Ligtenberg, S., van den Broeke, M., Nilsson, J., 2018. Increased West Antarctic and unchanged East Antarctic ice discharge over the last 7 years. *Cryosphere* 12 (2), 521–547. <https://doi.org/10.5194/tc-12-521-2018>.
- Graham, A.G.C., Larter, R.D., Gohl, K., Hillenbrand, C.-D., Smith, J.A., Kuhn, G., 2009. Bedform signature of a West Antarctic palaeo-ice stream reveals a multi-temporal record of flow and substrate control. *Quat. Sci. Rev.* 28, 2774–2793. <https://doi.org/10.1016/j.quascirev.2009.07.003>.
- Greene, C.A., Gwyther, D.E., Blankenship, D.D., 2017. Antarctic mapping tools for Matlab. *Comput. Geosci.* 104, 151–157. <https://doi.org/10.1016/j.cageo.2016.08.003>.
- Harig, C., Simons, F.J., 2015. Accelerated West Antarctic ice mass loss continues to outpace East Antarctic gains. *Earth Planet. Sci. Lett.* 415, 134–141. <https://doi.org/10.1016/j.epsl.2015.01.029>.
- Holland, C.W., Anandakrishnan, S., 2009. Subglacial seismic reflection strategies when source amplitude and medium attenuation are poorly known. *J. Glaciol.* 55 (193), 931–937. <https://doi.org/10.3189/002214309790152528>.
- Holschuh, N., Parizek, B.R., Alley, R.B., Anandakrishnan, S., 2017. Decoding ice sheet behavior using englacial layer slopes. *Geophys. Res. Lett.* 44 (11), 5561–5570. <https://doi.org/10.1002/2017gl073417>.
- Horgan, H.J., Anandakrishnan, S., Alley, R.B., Burkett, P.G., Peters, L.E., 2011. Englacial seismic reflectivity: imaging crystal-orientation fabric in West Antarctica. *J. Glaciol.* 57 (204), 639–650. <https://doi.org/10.3189/002214311797409686>.
- Jenkins, A., Dutrieux, P., Jacobs, S., Steig, E., Gudmundsson, H., Smith, J., Heywood, K., 2016. Decadal ocean forcing and Antarctic Ice Sheet response: lessons from the Amundsen Sea. *Oceanography* 29 (4), 106–117. <https://doi.org/10.5670/oceanog.2016.103>.
- Joughin, I., Tulaczyk, S., Bamber, J., Blankenship, D., Holt, J., Scambos, T., Vaughan, D., 2009. Basal conditions for Pine Island and Thwaites Glaciers, West Antarctica, determined using satellite and airborne data. *J. Glaciol.* 55 (190), 245–257. <https://doi.org/10.3189/002214309788608705>.
- Joughin, I., Smith, B.E., Holland, D.M., 2010. Sensitivity of 21st century sea level to ocean-induced thinning of Pine Island Glacier, Antarctica. *Geophys. Res. Lett.* 37, L20502. <https://doi.org/10.1029/2010GL044819>.
- Joughin, I., Smith, B.E., Medley, B., 2014. Marine Ice Sheet collapse potentially underway for the Thwaites Glacier Basin, West Antarctica. *Science* 344, 735–738. <https://doi.org/10.1126/science.1249055>.
- Kamb, B., 1991. Rheological nonlinearity and flow instability in the deforming bed mechanism of ice stream motion. *J. Geophys. Res.* 96 (B10), 16,585–16,595.
- King, E.C., Woodward, J., Smith, A.M., 2004. Seismic evidence for a water-filled canal in deforming till beneath Rutford Ice Stream, West Antarctica. *Geophys. Res. Lett.* 31, L20401. <https://doi.org/10.1029/2004GL020379>.
- King, E.C., Woodward, J., Smith, A.M., 2007. Seismic and radar observations of subglacial bed forms beneath the onset zone of Rutford Ice Stream, Antarctica. *J. Glaciol.* 53 (183), 665–672. <https://doi.org/10.3189/002214307784409216>.
- King, E.C., Hindmarsh, R.C.A., Stokes, C.R., 2009. Formation of mega-scale glacial lineations observed beneath a West Antarctic ice stream. *Nat. Geosci.* 2 (8), 585–588. <https://doi.org/10.1038/ngeo581>.

- Koellner, S., Parizek, B.R., Alley, R.B., Muto, A., Holschuh, N., 2018. The impact of spatially-variable basal properties on outlet glacier flow. In: *International Symposium on Timescales, Processes and Ice Sheet Changes*. Buffalo, NY, USA, 3–18 June.
- Leeman, J.R., Valdez, R.D., Alley, R.B., Anandakrishnan, S., Saffer, D.M., 2016. Mechanical and hydrologic properties of Whillans Ice Stream till: implications for basal strength and stick-slip failure. *J. Geophys. Res., Earth Surf.* 121. <https://doi.org/10.1002/2016JF003863>.
- Luthra, T., Peters, L.E., Anandakrishnan, S., Alley, R.B., Holschuh, N., Smith, A.M., 2017. Characteristics of the sticky spot of Kamb Ice Stream, West Antarctica. *J. Geophys. Res., Earth Surf.* 122 (3), 641–653. <https://doi.org/10.1002/2016JF004181>.
- MacAyeal, D.R., 1992. The basal stress distribution of Ice Stream E, Antarctica, inferred by control methods. *J. Geophys. Res.* 97 (B1), 595–603.
- Medwin, H., Clay, C.S., 1998. *Fundamentals of Acoustical Oceanography*. Academic Press, San Diego, CA, USA.
- Morlighem, M., Seroussi, H., Larour, E., Rignot, E., 2013. Inversion of basal friction in Antarctica using exact and incomplete adjoints of a higher-order model. *J. Geophys. Res., Earth Surf.* 118 (3), 1746–1753. <https://doi.org/10.1002/jgrf.20125>.
- Mouginot, J., Rignot, E., Scheuchl, B., 2014. Sustained increase in ice discharge from the Amundsen Sea Embayment, West Antarctica, from 1973 to 2013. *Geophys. Res. Lett.* 41, 1576–1584. <https://doi.org/10.1002/2013GL059069>.
- Nias, I.J., Cornford, S.L., Payne, A.J., 2016. Contrasting the modelled sensitivity of the Amundsen Sea Embayment ice streams. *J. Glaciol.* 62 (233), 552–562. <https://doi.org/10.1017/jog.2016.40>.
- Nitsche, F.O., Larter, R.D., Gohl, K., Graham, A.G.C., Kuhn, G., 2016. Crag-and-tail features of the Amundsen Sea continental shelf, West Antarctica. *Mem. Geol. Soc. Lond.* 46, 199–200. <https://doi.org/10.1144/M46.2>.
- Parizek, B.R., Christianson, K., Anandakrishnan, S., Alley, R.B., Walker, R.T., Edwards, R.A., Wolfe, D.S., Bertini, G.T., Rinehart, S.K., Bindschadler, R.A., Nowicki, S.M.J., 2013. Dynamic (in)stability of Thwaites Glacier, West Antarctica. *J. Geophys. Res., Earth Surf.* 118. <https://doi.org/10.1002/jgrf.20044>.
- Peters, L.E., Anandakrishnan, S., Holland, C.W., Horgan, H.J., Blankenship, D.D., Voigt, D.E., 2008. Seismic detection of a subglacial lake near the South Pole, Antarctica. *Geophys. Res. Lett.* 35, L23501. <https://doi.org/10.1029/2008GL035704>.
- Rathbun, A.P., Marone, C., Alley, R.B., Anandakrishnan, S., 2008. Laboratory study of the frictional rheology of sheared till. *J. Geophys. Res.* 113, F02020. <https://doi.org/10.1029/2007JF000815>.
- Rignot, E., Mouginot, J., Scheuchl, B., 2016. MEaSUREs Antarctic Grounding Line from Differential Satellite Radar Interferometry, Version 2. NASA National Snow and Ice Data Center Distributed Active Archive Center, Boulder, Colorado, USA. <https://doi.org/10.5067/IKBWW4RYHF1Q>. (Accessed 28 December 2016).
- Rignot, E., Mouginot, J., Scheuchl, B., 2017. MEaSUREs InSAR-Based Antarctica Ice Velocity Map, Version 2. NASA National Snow and Ice Data Center Distributed Active Archive Center, Boulder, Colorado, USA. <https://doi.org/10.5067/D7GK8F5J8M8R>. (Accessed 1 August 2018).
- Schoof, C., 2005. The effect of cavitation on glacier sliding. *Proc. R. Soc. Lond. Ser. A, Math. Phys. Sci.* 461 (2055), 609–627. <https://doi.org/10.1098/rspa.2004.1350>.
- Schroeder, D.M., Blankenship, D.D., Young, D.A., Quartini, E., 2014a. Evidence for elevated and spatially variable geothermal flux beneath the West Antarctic Ice Sheet. *Proc. Natl. Acad. Sci. USA*. <https://doi.org/10.1073/pnas.1405184111>.
- Schroeder, D.M., Blankenship, D.D., Young, D.A., Witus, A.E., Anderson, J.B., 2014b. Airborne radar sounding evidence for deformable sediments and outcropping bedrock beneath Thwaites Glacier, West Antarctica. *Geophys. Res. Lett.* 41. <https://doi.org/10.1002/2014GL061645>.
- Sheriff, R.E., Geldart, L.P., 1995. *Exploration Seismology*, 2nd ed. Cambridge University Press, Cambridge, UK.
- Smith, A.M., 1997. Basal conditions on Rutford Ice Stream, West Antarctica, from seismic observations. *J. Geophys. Res.* 102, 543–552.
- Smith, A.M., Murray, T., Davison, B.M., Clough, A.F., Woodward, J., Jiskoot, H., 2002. Late surge glacial conditions on Bakaninbreen, Svalbard, and implications for surge termination. *J. Geophys. Res.* 107 (B8), 2152. <https://doi.org/10.1029/2001JB000475>.
- Smith, A.M., 2007. Subglacial bed properties from normal-incidence seismic reflection data. *J. Environ. Eng. Geophys.* 12, 3–13.
- Smith, A.M., Murray, T., Nicholls, K.W., Makinson, K., Aðalgeirsdóttir, G., Behar, A.E., Vaughan, D.G., 2007. Rapid erosion, drumlin formation, and changing hydrology beneath an Antarctic ice stream. *Geology* 35 (2), 127–130. <https://doi.org/10.1130/G23036A.1>.
- Smith, A.M., Jordan, T.A., Ferraccioli, F., Bingham, R.G., 2013. Influence of subglacial conditions on ice stream dynamics: seismic and potential field data from Pine Island Glacier, West Antarctica. *J. Geophys. Res., Solid Earth* 118, 1471–1482. <https://doi.org/10.1029/2012JB009582>.
- Smith, B.E., Gourmelen, N., Huth, A., Joughin, I., 2017. Connected subglacial lake drainage beneath Thwaites Glacier, West Antarctica. *Cryosphere* 11 (1), 451–467. <https://doi.org/10.5194/tc-11-451-2017>.
- Spagnolo, M., Bartholomaeus, T.C., Clark, C.D., Stokes, C.R., Atkinson, N., Dowdeswell, J.A., Ely, J.C., Graham, A.G.C., Hogan, K.A., King, E.C., Larter, R.D., Livingstone, S.J., Pritchard, H.D., 2017. The periodic topography of ice stream beds: insights from the Fourier spectra of mega-scale glacial lineations. *J. Geophys. Res., Earth Surf.* 122 (1), 1–12. <https://doi.org/10.1002/2016JF004154>.
- Taylor, B.N., Kuyatt, C.E., 1994. Guidelines for evaluating and expressing the uncertainty of NIST measurement results. In: *NIST Technical Note 1297 1994 Edition*. National Institute of Standards and Technology, Gaithersburg, MD, US.
- Tulaczyk, S., Kamb, B., Engelhardt, H.F., 2001. Estimates of effective stress beneath a modern West Antarctic ice stream from till preconsolidation and void ratio. *Boreas* 30 (2), 101–114. <https://doi.org/10.1080/030094801750203134>.
- Vaughan, D.G., Smith, A.M., Nath, P.C., Le Meur, E., 2003. Acoustic impedance and basal shear stress beneath four Antarctic ice streams. *Ann. Glaciol.* 36, 225–232. <https://doi.org/10.3189/172756403781816437>.
- Walker, R.T., Christianson, K., Parizek, B.R., Anandakrishnan, S., Alley, R.B., 2012. A viscoelastic flowline model applied to tidal forcing of Bindschadler Ice Stream, West Antarctica. *Earth Planet. Sci. Lett.* 319–320, 128–132. <https://doi.org/10.1016/j.epsl.2011.12.019>.
- Weertman, J., 1957. On the sliding of glaciers. *J. Glaciol.* 3 (21), 33–38.